UCLA
COMPUTATIONAL AND APPLIED MATHEMATICS

Noise Removal Using Fourth-Order Partial Differential Equations with Applications to Medical Magnetic Resonance Images in Space and Time

Marius Lysaker

Arvid Lundervold

Xue-Cheng Tai

July 2002

CAM Report 02-44

Noise Removal Using Fourth-Order Partial Differential Equations with Applications to Medical Magnetic Resonance Images in Space and Time

Marius Lysaker, Arvid Lundervold, Xue-Cheng Tai

M. Lysaker and X-C. Tai are with the Department of Mathematics, University of Bergen, Johannes Brunsgate 12, N-5009 Bergen, Norway (e-mail: {mariusl,tai}@mi.uib.no). A. Lundervold is with the Department of Physiology and Department of Clinical Engineering (Haukeland University Hospital), University of Bergen, Aarstadveien 19, N-5009 Bergen, Norway (e-mail: Arvid.Lundervold@fys.uib.no).

Abstract

In this paper we introduce a new method for image smoothing based on a fourth order PDE model. The method is tested on a broad range of medical magnetic resonance images, both in space and time, as well as on non-medical test images. Our algorithm demonstrates good noise suppression with preservation of edges and contours and without destruction of important anatomical or functional detail, even at poor signal-to-noise ratios. We have also compared our method with a related second-order PDE model and find our method to perform overall better on the images being tested.

Keywords

Noise removal, MRI, PDE.

I. Introduction

During the last two decades progress in medical magnetic resonance imaging (MRI) technology has created a large collection of imaging techniques, so-called pulse sequences, available to both clinicians and researchers. Each such pulse sequence exploits some specific physical or chemical property of the hydrogen nuclei (protons) of small, mobile molecules like water and certain lipids, and can depict structural and functional information from living tissue at the sub-millimeter scale.

Even if the scanner technology has undergone tremendous improvements in spatial resolution, acquisition speed, and signal-to-noise ratio, MR images are still hampered with degradations like signal intensity inhomogeneities (bias fields), noise, and other artifacts. One of the limiting factors regarding performance and usefulness of quantitative MRI diagnostics, such as voxel-based tissue classification, extraction of organ shape or tissue boundaries, estimation of physiological parameters, e.g. tissue perfusion and contrast agent permeability from dynamic imaging, is the amount of noise in the acquisitions. A major source of this type of image degradation is random thermal noise entering the MR data in the time domain [1] (explained in more detail in Section II).

To overcome the deficiencies of so-called *acquisition-based noise reduction*, such as increased acquisition time (i.e. time averaging over repeated measurements) or decreased spatial resolution (i.e. enlarging voxel volume), several *post-processing noise reduction* methods have been proposed.

The ultimate goal of post-scanning noise removal methods in MRI is to obtain piecewise constant, or slowly varying signals in homogeneous tissue regions while preserving tissue boundaries. Over the years, many different noise suppression methods have been proposed. However, there is no single method that has shown to be superior to all the others regarding goodness of noise removal, boundary preservation, robustness, user interaction, applicability to the different MR acquisitions techniques, and computation cost. Thus, improvements are still needed.

In the literature, both statistical approaches and diffusion filter methods have been used to remove noise from digital images. An early study of "image improvement" in MRI using statistical approach has been done in Godtliebsen [2] (see also [3], [4]). Using Markov field models with maximum a posteriori (MAP) estimation of restored intensity values by iterated conditional modes (ICM) and simulated annealing (SA), it was found that application of the best of these methods to an average of two measurements gave an image of about the same quality as an average of four single measurements. Moreover, the noise characteristics in spin echo T_1-weighted transverse images of the head (Fourier reconstructed magnitude images) was investigated and it was found that the noise distribution was normal with zero mean, that the noise in different pixels was uncorrelated, and that the noise did not depend on the signal intensity level.

Soltanian-Zadeh and coworkers [5] have introduced an edge preserving, nonlinear filter for multispectral (vector-valued) MR image restoration that uses the zero-mean white Gaussian model for statistical noise. Their filter considers a neighborhood around each pixel and needs specification of a threshold value for Euclidean distances between pixel vectors based on noise standard deviation in the images, the contrast between adjacent tissues, and partial volume averaging effects which are reflected in the sharpness of edges in each image. Their noise suppression algorithm has been applied as part of preprocessing in image segmentation and tissue characterization of brain tumors ([6]), but is not widely used partly because it is restricted to multispectral MR image acquisitions.

On the other hand, considerable research interest and numerous applications in MRI has been devoted to use nonlinear diffusion filters, see [7], [8], [9], [10], [11], [12], [13], [14], [15], [16], [17], [18], [19], [20], [21]. One of the common features of the nonlinear diffusion

filters is to introduce a nonlinear diffusion term where the diffusion coefficient $g(|\nabla u|^2)$ is small when the gradient (i.e. $|\nabla u|$) is large. The images are filtered by examining their evolutions under nonlinear partial differential equations (PDEs). In contrast to linear diffusion filtering i.e. Gaussian filtering, which is hampered with blurring and localization problems, the nonuniform (anisotropic) process reduces the diffusibility at locations which have a larger likelihood of being edges by using the "edge-stopping" function $g(|\nabla u|^2)$. This idea was introduced in Perona-Malik [7] and it has been generalized to 3D images by Gerig et al. [8], and to vector-valued images by Sapiro and Ringach (1996), making it suitable to both 3D MRI and multispectral MRI.

Black et al. [9] studied the relation between anisotropic diffusion and robust statistics. They implemented a robust estimation procedure that estimates a piecewise smooth image from a noisy input image and demonstrated improved automatic stopping of the diffusion process with preservation of sharper boundaries and better continuity of edges compared to the Perona-Malik method. Their rationale for applying robust statistics to anisotropic diffusion was from the case of piecewise-constant images but was not extended to more general ones, like MRI, where there can be regions with slowly varying signal intensities and unsharp tissue boundary zones due to partial volume effects.

It seems that Rudin-Osher-Fatemi [11] was the first one to observe that if we minimize the total variation (TV) norms of the images under some given conditions, we will get some nonlinear diffusion filters. This idea gives a rigorous mathematical tool to introduce nonlinear diffusion filters and it has been used as a regularization method for many other applications where one needs to identify discontinuous functions. Motivated by the TV filter, many other similar filters have been proposed in the literature, see (e.g.[12], [13], [14], [15], [16], [17], [18], [19], [20], [21], etc.), The approach we shall take belongs to this class of filters. We shall introduce a fourth-order PDE noise suppression method that preserves boundaries and edges and works on 1D signals, as well as 2D, 3D and 3D+time images. The main motivation for introducing the new filters is to overcome the over-smoothing effect of the TV-norm filters, see Figure 6. The TV filters are able to remove noise and preserve edges. However, they also smooth out some of the fine details in non-blocky images. The method we shall propose has better capabilities in preserving some

of the fine details while also is able to smooth out noise and preserve edges. In order to test its practical potential we have applied our method to a wide range of real images, including structural and functional MRI data sets. Compared with some other fourth order nonlinear filters, see [17], [19], [21], [22], our approach is simpler and we only need to know the approximate noise level to determine how much diffusion we need to add. In [23], they try to reconstruct some 3D surfaces. The normal vectors for the surfaces are smoothed first and a surface is then chosen to fit the smoothed normal vectors. This process can be regarded as a two-step realization of a fourth order method which seems to be an interesting variant for the approach we are propsing here.

The rest of this paper is organized as follows. Since MRI is main target for our noise-removal method, giving rise to many image processing applications, we give in Section II a short review of the principles of MR Fourier transform image formation and how noise is introduced into the reconstructed images. Section III introduces a general formulation of the PDE model and in Section IV the Fourth-Order PDE is adapted to this framework. Section V explains the numerical solution we have employed. In order to compare the performance of our noise-suppression method with similar approaches, we have implemented the second- order PDE model by Rudin et al. [11], and both models are then tested using standard images with added noise. This comparison is reported in Section VI. In Section VII we test our method more extensively. Firstly, on synthesized images and natural scenes, then on a broad range of MR images obtained from MR phantoms, healthy volunteers and patients. The test images are acquired on clinical scanners from two different MR laboratories, and challenges our method by containing various amount of noise and structural detail. To investigate the potential clinical applicability of our method, we have selected both 2D and 3D anatomical images as well as time series (1D signals) of functional images from a routine brain perfusion examination. Finally, in Section VIII we discuss our findings and propose some directions for follow-up. This work is an extension of the thesis [24].

II. MR IMAGE FORMATION AND NOISE

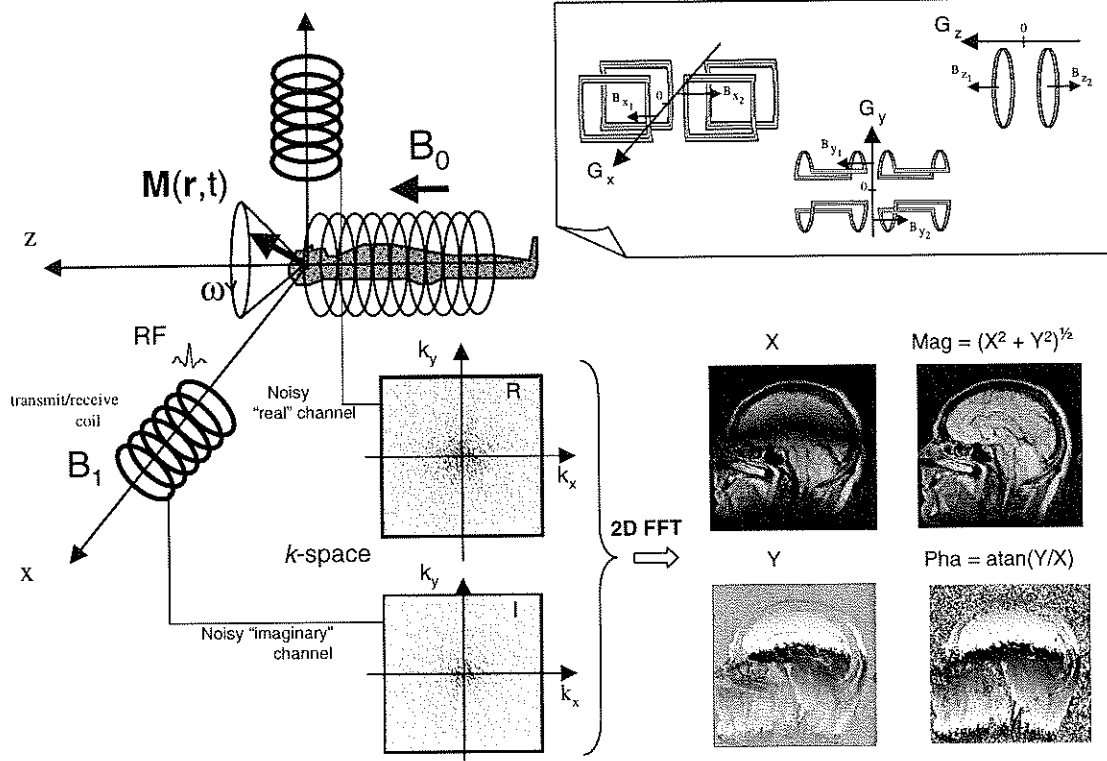The following figure illustrates the principles of 2D Fourier transform imaging on clinical MR scanners.

Fig. 1.   **Principles of MR image formation.** *In MRI we are sampling complex-valued signals $S(k_x, k_y)$ in the spatial frequency domain (k-space), being time-domain signals from two independent electronic sources (here denoted the "real" and "imaginary" channel). The signal values in k-space (i.e. raw data) can be expressed as $S(k_x, k_y) = \iint \rho(x,y) \exp\{-i(x\,k_x + y\,k_y)\}\,dx\,dy$, where $\rho(x,y)$ is the spatial distribution of proton spin density that we want to measure. "Filling" of k-space is done by designing k-space trajectories, $t \mapsto (k_x(t), k_y(t)) = \gamma(\int_0^t G_x(\tau)\,d\tau, \int_0^t G_y(\tau)\,d\tau)$, where the functions $G_x(t)$ and $G_y(t)$ are programmable time courses of the magnetic field gradients (cf. the coils in upper right insert). γ is the gyromagnetic ratio of the imaged nucleus (protons). Thus, during an imaging examination k-space is traversed by proper activation of the gradient system. Usually, k-space points are separated by Δk_x and Δk_y in the two orthogonal directions, and the NMR signals can be sampled on a regular 2D grid. We see from the first equation above, that spatial distribution of proton spin density $\rho(x,y)$ in complex-valued image space (X and Y images), and the NMR signal $S(k_x, k_y)$ in complex-valued spatial frequency space (R and I data matrices) define a Fourier pair. Thus, the image of proton spin densities (and other tissue properties such as spin-spin and spin-lattice relaxation) can be formed by applying a discrete, inverse Fourier transform to the data matrix of k-space samples. Generalization to 3D imaging involves application of the third gradient coil $(G_z(t))$ in the same fashion. For visual inspection or further processing the magnitude image (Mag) is used, and sometimes also the phase image (Pha) (with possible phase unwrapping). B_0 denotes the static magnetic field. $M(\mathbf{r}, t)$ is the magnetization vector at position $\mathbf{r}$, rotating at (resonance) frequency $\omega = \gamma B$. The total magnetic field $\mathbf{B}$ is under control of the pulse sequence program activating the gradient- and RF (radio-frequency) coils. In receive mode, these coils (in quadrature) are also used to pick up the weak NMR signals.*

Today, variations of this *Fourier transform imaging* technique is the most widespread MR method for obtaining structural and functional information from the living human body.

Noise in MRI enters the data samples in k-space. Here the noise voltage competes with the NMR signal and is due to random fluctuations in the receiving coil electronics and in the patient body (e.g. Brownian motion of spins). The variance of this thermal noise can be described as the sum of noise variances from independent stochastic processes, representing the body, the coil and the electronics [1], i.e.

$$\sigma^2_{\text{thermal}}(k_x, k_y) = \sigma^2_{\text{body}}(k_x, k_y) + \sigma^2_{\text{coil}}(k_x, k_y) + \sigma^2_{\text{electronics}}(k_x, k_y)$$

The noise-removal obtained by averaging n measurements, where noise in k-space is additive i.i.d. zero-mean Gaussian with standard deviation σ, yields an improvement in noise standard deviation of $\sigma_n = \sigma/\sqrt{n}$. This procedure of averaging, on expence of measurement time, is used in the experimental part of this paper to obtain the "true" MR image to compare our method with. Notice that in reconstructed magnitude images, the images used in most medical applications, the noise will generally not be Gaussian distributed. This is because computation of the magnitude image from the real and imaginary image, reconstructed by the inverse Fourier transform, involves a non-linear operation which maps a Gaussian distribution to a Rician distribution (e.g. [25]). Moreover, at high SNR the Rician distribution approaches the Gaussian distribution, and at low SNR it tends to be the Rayleigh distribution. Thus, there are signal-dependent noise characteristics in reconstructed magnitude MR images. However, our noise suppression PDE method, like most other de-noising methods, does not incorporate these noise-statistics subtilities in the model (but see [26] for a "Rician noise" model using wavelets), and we have used addition of i.i.d Gaussian noise in the experiments with non-medical test images to evaluate our algorithm.

For more details on MR imaging principles and the presence of noise, see [1], [27], [28], [29], [30], [31], [32].

III. PDE-DENOISING

Let $u(x, y)$ be the true image and $u_0(x, y)$ be its observation with random noise $\eta(x, y)$ for $x, y \in \Omega$. The noise model is then

$$u_0(x, y) = u(x, y) + \eta(x, y).$$

In the following we assume that the noise level is approximately known, i.e.

$$\int_\Omega (u - u_0)^2 \, dx \, dy \approx \sigma^2. \tag{1}$$

Noise is recognized as fast oscillating signals over small areas. One of the essential ideas for denoise digital images is to filter out the high frequency signals while preserve the other important features of the images. Different functionals can be used to measure the oscillations in the images. Lets us denote this operator $R(u)$. Examples of functionals that can be found in the literature are $R(u) = \int_\Omega g(u) \, dx$, with $g(u) = |\nabla u|$ or $g(u) = |\Delta u|$.

A general formulation of the noise removal problem is then to solve (c.f. [19], [11])

$$\begin{aligned} &\min \, R(u) \\ &\text{subject to (1)} \end{aligned} \tag{2}$$

The denoise version of the observed image is given by minimizing the objective $R(u)$ (i.e a measure of the oscillations in the image) subject to constrains involving the statistics of the noise.

Different functionals for $R(u)$ have been proposed in the literature. In Rudin-osher-Fatemi [11], $R(u)$ is taken as $R(u) = \int_\Omega |\nabla u| dx$. In [13], [16], [17], some modified TV-norm filters were applied. In Chan, Marquina and Mulet [19], they have used

$$R(u) = \int_\Omega \left(\alpha |\nabla u|_\beta + \mu \frac{\mathcal{L}(u)^2}{|\nabla u|_\gamma^3} \right) dx. \tag{3}$$

As the functionals get more and more complex, the computing time grows as well. It is important to keep in mind the relationship between the computing time and the requirement of accuracy in the result. In 1D and 2D images this is not an important issue, but as the number of unknown increases, the choice of functionals will have an significant impact on the computing time.

In medical diagnostics, 2D+time, 3D and 3D+time MR images are used, and the denoising process is quite expensive. We therefore propose an operator with an all over good trade-off between noise removal, edge preservation and computing time.

IV. FOURTH-ORDER PDE

We shall present the method only for $2D$ problems, but a generalization to $2D + time$, $3D$ and $3D + time$ is straight forward. The numerical experiments will be done not only for $2D$, but also for $2D + time$ and $3D$ problems. In our proposed algorithms, we shall use the following operator as a measure of the oscillations:

$$R(u) = \int_\Omega (|u_{xx}| + |u_{yy}|) \, dx \, dy \qquad x, y \in \Omega. \tag{4}$$

In the original TV-norm filter [11], one is trying to minimize the total variation norm of the function u. Here, we are essentially trying to minimize the total variation norm of the gradient ∇u. But, for simplicity for the implementation, we have dropped some of the terms with mixed derivatives. In section VI, we shall give an explanation about the advantages using this measurement.

Suppose that the noise level σ^2 in the image u_d is approximately known as in (1). We are now trying to get at new image u that solves the minimization problem (2), i.e. we are trying to minimize a semi-norm of the second order derivative under the noise level constraint. A technique for finding minimum values of (4) subject to the noise level constraint (1) are based on a Lagrangian function

$$L(u, \lambda) = \int_\Omega (|u_{xx}| + |u_{yy}|) \, dx \, dy + \frac{1}{2}\lambda(\int_\Omega (u - u_d)^2 \, dx \, dy \, - \sigma^2). \tag{5}$$

At any critical point of $L(u, \lambda)$ we must have

$$\frac{\partial L}{\partial \lambda} = 0, \quad \frac{\partial L}{\partial u} \cdot v = 0, \ \forall v.$$

Here, the differentiation means Gauteaux derivatives. This first optimality condition gives

$$0 = \frac{\partial L}{\partial \lambda} = \frac{1}{2} \int_\Omega (u - u_d)^2 \, dx \, dy \, - \frac{1}{2}\sigma^2 \tag{6}$$

and this essentially recovers constraint (1). From the definition of $L(u, \lambda)$, it is easy to calculate that

$$\frac{\partial L}{\partial u} \cdot v = \int_\Omega \left(\frac{u_{xx}}{|u_{xx}|} v_{xx} + \frac{u_{yy}}{|u_{yy}|} v_{yy} \right) \, dx \, dy + \lambda \int_\Omega (u - u_d)v \, dx \, dy. \tag{7}$$

By using integration by part twice on (7), the second optimality condition implies that u satisfies the following nonlinear partial differential equation

$$\left(\frac{u_{xx}}{|u_{xx}|}\right)_{xx} + \left(\frac{u_{yy}}{|u_{yy}|}\right)_{yy} + \lambda(u - u_d) = 0 \ \text{ in } \Omega \tag{8}$$

and the boundary condition is given by

$$a) \ \left(\frac{u_{xx}}{|u_{xx}|}\right)n_1 + \left(\frac{u_{yy}}{|u_{yy}|}\right)n_2 = 0, \qquad b) \ \left(\frac{u_{xx}}{|u_{xx}|}\right)_x n_1 + \left(\frac{u_{yy}}{|u_{yy}|}\right)_y n_2 = 0 \ \text{ on } \partial\Omega \tag{9}$$

where $\mathbf{n} = (n_1, n_2)$ is the normal direction on $\partial\Omega$.

Different methods for solving the nonlinear equation (8) are available and we have chosen to use a parabolic equation with time as an evolution parameter. This means that we solve for $t > 0$, $x, y \in \Omega$

$$u_t = -\left(\frac{u_{xx}}{|u_{xx}|}\right)_{xx} - \left(\frac{u_{yy}}{|u_{yy}|}\right)_{yy} - \lambda(u - u_d). \tag{10}$$

By introducing time as an evolution parameter the nonlinear equation (8) can be solved by using an explicit difference method for (10). As t increases, steady state will be reached and we get the denoised version of our image.

V. DIFFERENCE EQUATION

A typical digital image is often defined on a rectangular domain Ω with a regular mesh

$$x = i\Delta x \quad i = 0, 1, ...I$$
$$y = j\Delta y \quad j = 0, 1, ...J.$$

For image problems, we will take $\Delta x = 1, \Delta y = 1$ and $I \times J$ is the size of image support.

The iteration requires a start image u_{init}, and we use $u_{init} = u_d$. Choose a time step Δt, the numerical approximation of (10) could be given by

$$u^{l+1} = u^l - \Delta t D_{xx}\left[\alpha(u^l)D_{xx}u^l\right] - \Delta t D_{yy}\left[\beta(u^l)D_{yy}u^l\right] - \Delta t\lambda^l(u^l - u_d), \tag{11}$$

here

$$(D_{xx}u)_{i,j} = \frac{u_{i-1,j} - 2u_{i,j} + u_{i+1,j}}{\Delta x^2}, \qquad (D_{yy}u)_{i,j} = \frac{u_{i,j-1} - 2u_{i,j} + u_{i,j+1}}{\Delta y^2}. \tag{12}$$

and $\alpha(u) = \frac{1}{|D_{xx}u|}$, $\beta(u) = \frac{1}{|D_{yy}u|}$.

It is easy to see that

$$\alpha(u)D_{xx}u = \begin{cases} 1 & \text{if } u \text{ is convex with respect to } x \\ \text{undefined} & \text{if } u \text{ is linear with respect to } x \\ -1 & \text{if } u \text{ is concave with respect to } x \end{cases} \qquad (13)$$

If the image is planar in some region we get a zero divide in $\alpha(u)$- and $\beta(u)$-term. To avoid this problem a small parameter $\epsilon > 0$ is introduced and replace $\alpha(u)$ and $\beta(u)$ by $\overline{\alpha}(u) = \frac{1}{|D_{xx}u|+\epsilon}$ and $\overline{\beta}(u) = \frac{1}{|D_{yy}u|+\epsilon}$ respectively. It is clear that

$$\overline{\alpha}(u)D_{xx}u \begin{cases} \leq 1 & \text{if } u \text{ is convex with respect to } x \\ = 0 & \text{if } u \text{ is linear with respect to } x \\ \geq -1 & \text{if } u \text{ is concave with respect to } x \end{cases} \qquad (14)$$

Numerical tests show that the value of ϵ is not critical, but this parameter should not be significant compared with $D_{xx}u$ unless u is almost planar, and therefore we have chosen $\epsilon = 10^{-2}$.

To incorporate the boundary conditions (9), the approximations at the boundaries need to be treated properly. To explain it in detail, let's introduce two functions $s(u) = \overline{\alpha}(u)D_{xx}u$, $f(s) = D_{xx}s$. In the implementations, the values of s and f for a given function u are evaluated according to the following formulas:

$$(s(u))_{i,j} = \begin{cases} \overline{\alpha}(u)_{i,j}(D_{xx}u)_{i,j} & \text{if } 1 < i < I, \\ 0 & \text{if } i = 1, \text{ or } I. \end{cases} \qquad (15)$$

$$(f(s))_{i,j} = \begin{cases} (D_{xx}s)_{i,j} & \text{if } 1 < i < I, \\ \frac{2}{\Delta x^2}(s_{i+1,j} - s_{i,j}) & \text{if } i = 1, \\ \frac{2}{\Delta x^2}(s_{i-1,j} - s_{i,j}) & \text{if } i = I. \end{cases} \qquad (16)$$

In (15), boundary condition (9.a) is incorporated and in (16), boundary condition (9.b) is incorporated. Similar treatment should be done for the y-spatial variable.

Under the assumption that steady state has been reached, a combination of (10) and the approximated noise level (1) gives a dynamic updating of λ. By multiplying (10) by $(u - u_d)$ and integrating by parts twice over Ω we then have

$$\lambda = -\frac{1}{\sigma^2} \int_{\Omega} \frac{u_{xx}}{|u_{xx}|}(u - u_d)_{xx} \, dx \, dy - \frac{1}{\sigma^2} \int_{\Omega} \frac{u_{yy}}{|u_{yy}|}(u - u_d)_{yy} \, dx \, dy. \qquad (17)$$

Numerically $\frac{u_{xx}}{|u_{xx}|}$ is approximated by (15) and $(u - u_d)_{xx}$ by (12). In each iteration (17) is used to update λ in (11), i.e.

$$\lambda^l = -\frac{1}{\sigma^2} \int_\Omega \frac{u_{xx}^l}{|u_{xx}^l| + \epsilon}(u^l - u_d)_{xx} \, dx \, dy \; - \frac{1}{\sigma^2} \int_\Omega \frac{u_{yy}^l}{|u_{yy}^l| + \epsilon}(u^l - u_d)_{yy} \, dx \, dy. \qquad (18)$$

VI. THE FOURTH ORDER PDE COMPARED WITH A SECOND ORDER PDE

In this work, we shall only compare our proposed algorithm with the well-known algorithm of [11]. To explain why our scheme has better properties than the scheme of [11], we shall consider the schemes for one dimensional problems. The scheme of [11] is obtained by choosing the $R(u)$ functional as $R(u) = \int_\Omega |\nabla u| dx$. Correspondingly, in the one dimensional case and for a given noisy image v_{init}, the algorithm of [11] takes the following form:

$$\frac{v^{l+1} - v^l}{\Delta t} = \frac{\partial}{\partial x}\left(\frac{1}{|v_x^l|}\frac{\partial v^l}{\partial x}\right) - \lambda^l(v^l - v_{init}) \qquad (19)$$

Our scheme reduces to the following for one dimensional problems:

$$\frac{u^{l+1} - u^l}{\Delta t} = -\frac{\partial^2}{\partial x^2}\left(\frac{1}{|u_{xx}^l|}\frac{\partial^2 u^l}{\partial x^2}\right) - \lambda^l(u^l - u_{init}) \qquad (20)$$

Both algorithms are trying to remove noise the initial values. To see what kind of fundamental differences these two updating formula may have, we look at two related linear parabolic equations in the one-dimensional case, i.e. we consider

$$\left.\begin{array}{ll} v_t = v_{xx} & v(0) = v(1) = 0 \\ u_t = u_{xxxx} & u(0) = u_x(0) = u(1) = u_x(1) = 0 \end{array}\right\} x \in (0,1), t > 0 \qquad (21)$$

These equations are the one dimensional counter part of equations (19) and (20) taking $\lambda = 0$ and fixing the nonlinear diffusion coefficient $\alpha(u)$ and $\beta(u)$ to be 1.

By using separation of variables we get

$$\frac{T'(t)}{T(t)} = \frac{\chi''(x)}{\chi(x)} = -\omega^2 \quad \text{and} \quad \frac{T'(t)}{T(t)} = \frac{X''''(x)}{X(x)} = -\gamma^4 \quad \text{with } \omega > 0, \gamma > 0. \qquad (22)$$

Thus, the solutions for the two linear equations of (21) should have the following forms:

$$v(x,t) = \sum_{n=1}^\infty \chi_n(x)e^{-(n\pi)^2 t} \quad \text{and} \quad u(x,t) = \sum_{n=1}^\infty X_n(x)e^{-(n\pi)^4 t}, \qquad (23)$$

with

$$\chi_n(x) = \overline{A}_n \cos(n\pi x) + \overline{B}_n \sin(n\pi x) \ ,$$

and

$$X_n(x) = A_n \cos(n\pi x) + B_n \sin(n\pi x) + C_n \cosh(n\pi x) + D_n \sinh(n\pi x).$$

The coefficients in $\chi_n(x)$ and $X_n(x)$ are chosen to satisfy the initial and boundary conditions. Suppose the initial values $v(x,0)$ and $u(x,0)$ are composed of signals of different frequencies, i.e. $v(x,0) = \sum_{n=1}^{\infty} \overline{B}_n \sin(n\pi x)$ and $u(x,0) = \sum_{n=1}^{\infty} B_n \sin(n\pi x)$. Then the solutions of (21) are given by

$$v(x,t) = \sum_{n=1}^{\infty} \overline{B}_n sin(n\pi x)e^{-(n\pi)^2 t} \quad \text{and} \quad u(x,t) = \sum_{n=1}^{\infty} B_n sin(n\pi x)e^{-(n\pi)^4 t}. \quad (24)$$

For a given frequency $\sin(n\pi x)$, the signal is damped out by a factor $e^{-(n\pi)^2 t}$ at time t by the second order parabolic equation and it is damped out by a factor $e^{-(n\pi)^4 t}$ at time t by the fourth order parabolic equation. Thus the fourth order partial differential equation removes high frequency noise from the initial value faster than the second order parabolic equation. It is expected that the nonlinear updating formula (19) and (20) would also have some of the properties of the corresponding linear equations.

By a similar argument as given above it is easy to show that a 2m'th order PDE is able to damp out a frequency $\sin(n\pi x)$ by a factor $e^{-(n\pi)^m t}$. Higher order PDE's damp out signal with high frequency faster, but there is also some drawbacks. Let us consider the following 2m'th order parabolic equation in 1D:

$$u_t = \left(\frac{u_m}{|u_m| + \epsilon}\right)_m, \quad \text{with some proper boundary condition.}$$

Here u_m denotes the m'th order derivative of u. The term $\left(\frac{u_m}{|u_m|+\epsilon}\right)_m$ acts as a penalty term to oscillation, and for $m = 1$ the right hand side equals zero if u is constant. If $m = 2$ the penalty term equals zero also if u is linear, and for $m = 3$ the penalty term is zero when u is quadratic.

Assume we want to identify a homogeneous region which is exposed with noise. There is no reason to expect that $m = 2,3$ is able to do a better job than $m = 1$. On the other hand, we shall expect that $m = 2,3$ would give a better result for non-blocky images. One

question is that the higher order smoother is really better than the corresponding lower order smoother or not and this should be answered in one numerical experiment in the next section.

VII. EXPERIMENTAL RESULTS

A. Synthesized images and natural scenes

To compare the effect for the schemes with different m's, we have implemented and tested the second order (19), the fourth order (20) and the sixth order scheme in 1D. A test image of constant, linear and curved regions is used. It is important to note that all parameters (stepsize in time and space, noise level and ϵ) in the algorithm were identical, except for the smoother during this evaluation.

(a) Original curve

(b) Noisy curve

(c) m=1

(d) m=2

(e) m=3
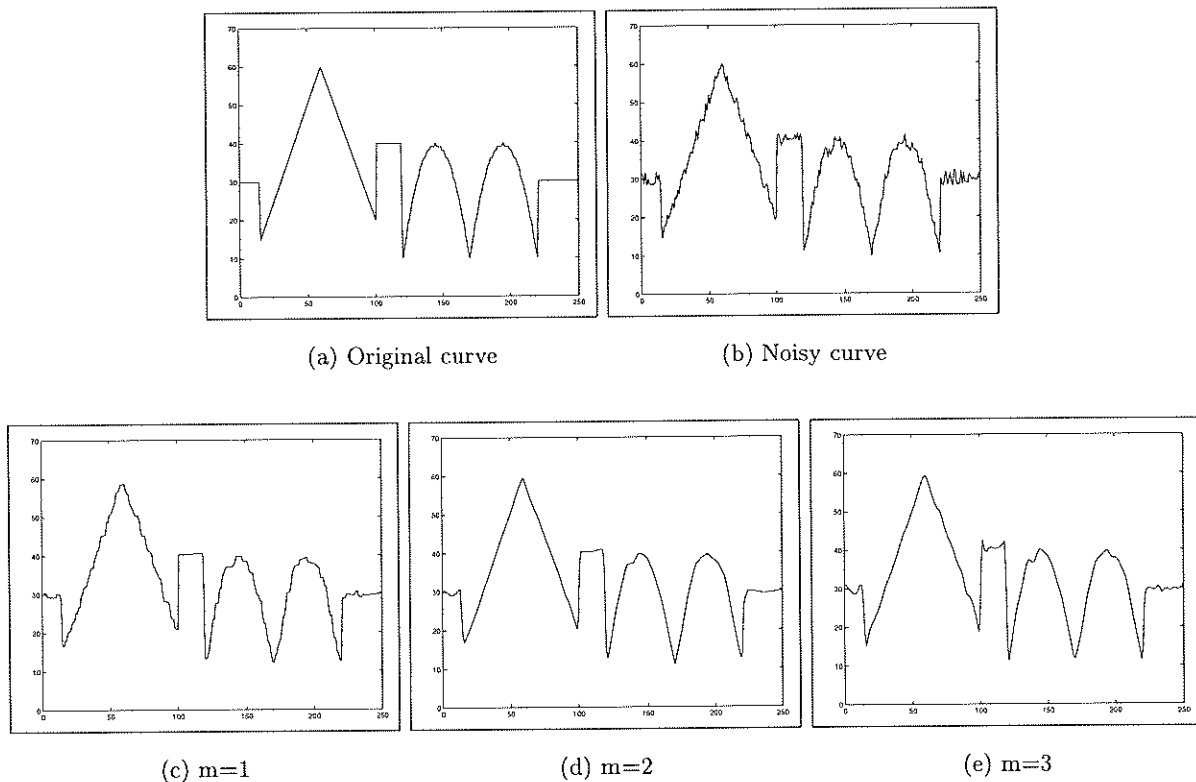
Fig. 2. 1D image evaluation

The experimental results are displayed in Figure 2. As expected the staircase effect is visible for $m = 1$. Higher order schemes do not have the stair-case effect, but for $m = 3$

we are not able to identify homogeneous region that well, as seen from the bars at (0,20) and (100,120).

We have carried out different tests. For $m = 1$, the obtained images always suffer from starcase-effect and over-smoothing or so called oil-painting effect. For $m = 3$, it is able to overcome the problems associated with $m = 1$, but it is also producing oscillations in homogeneous regions. The scheme with $m = 2$ seems to have a good balance between these things.

In Figure 3, we report some 2D experimental results. One of the purposes for this experiment is to show that the fourth order scheme, i.e. the scheme with $m = 2$, works as good as the second order scheme (i.e. $m = 1$) even when the image is blocky, i.e. the image is piecewise contants. Some of the blocks are as small 2x2 pixels and other as thin as 1x10 pixels. The second order scheme is known to work for this kind of images. Our new fourth order scheme works also very well.

(a) Original image

(b) Noisy image

(c) 4-order PDE

(d) 2-order PDE

Fig. 3. 2D image evaluation with different PDE's

(a) Original image   (b) Noisy image

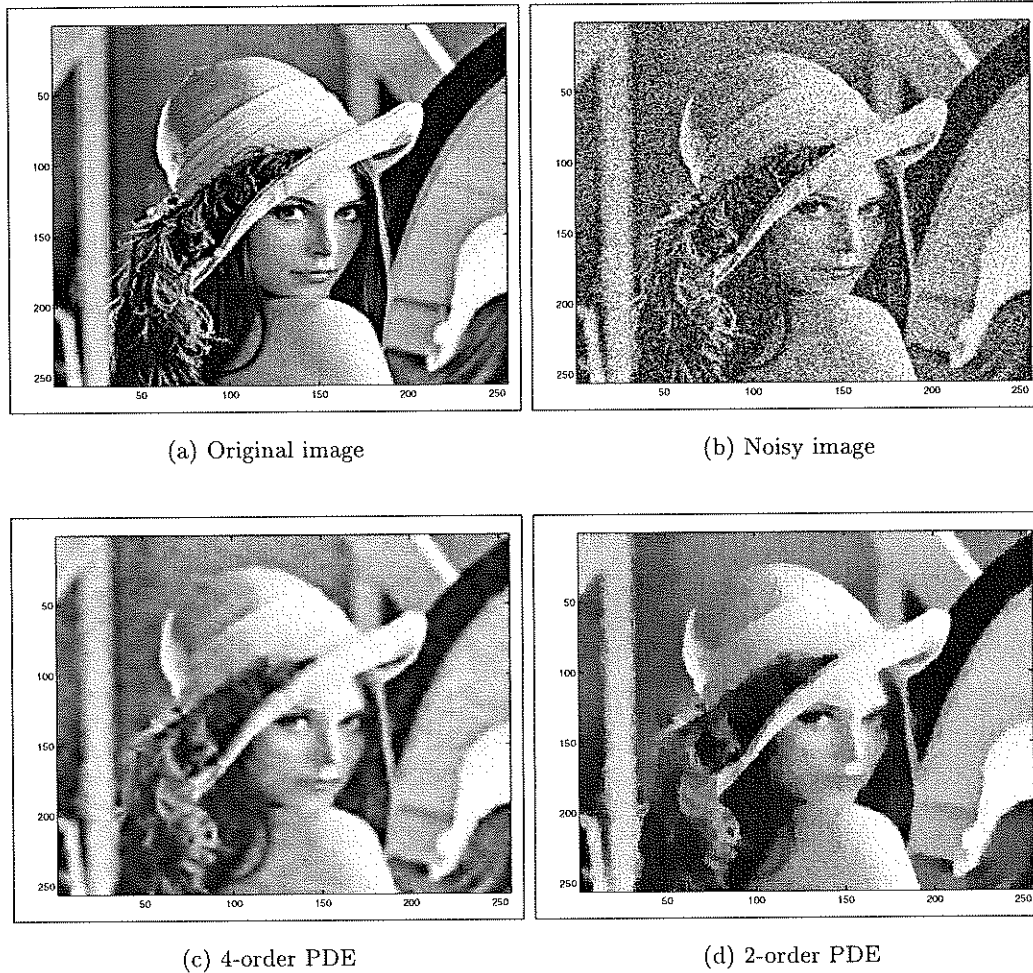(c) 4-order PDE   (d) 2-order PDE
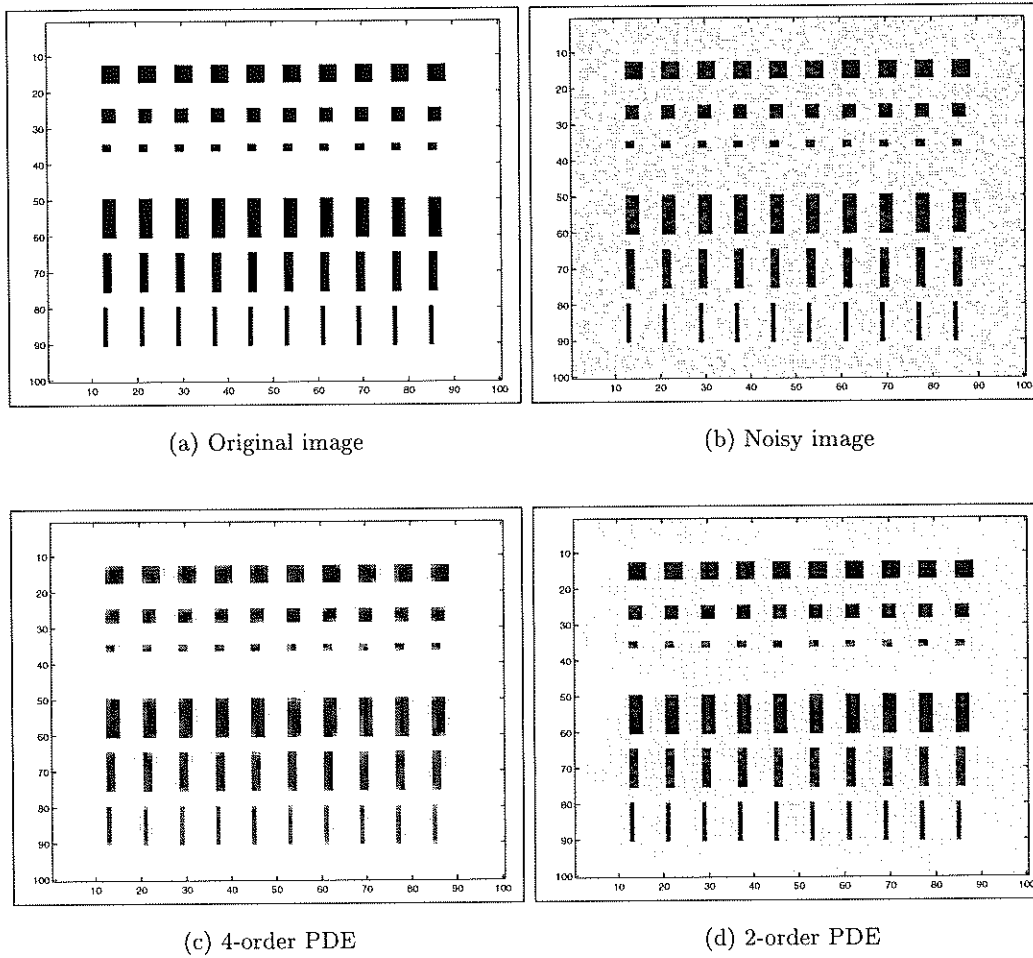
Fig. 4. 2D image evaluation with different PDE's

In the next test, we use the noisy version of the well known Lena image as input data. From Fig. 4 it is easy to see that the second-order PDE is able to smooth out almost all noise, but unfortunately, some of the contrast in the image as well. On the other hand, the fourth-order PDE seems to preserve all the important information in the image, but also some of the noise. To choose the desired PDE to solve the restoration problem among the second- and fourth-order PDE, an evaluation of the trade-off between noise removal and edge preservation is done. For this evaluation a special test image is used. Noise is only introduced in one half of the image, depicted in Fig. 5. The restoration algorithm should now do little or nothing in the left part (edge preservation) and reconstruct a denoised version of the right part.

Fig. 5. Noise introduced in right part

A contour plot is used to visualize the ability to detect edges and remove noise, see Figure 6. It is obvious that the contours shown in the left part of Fig. 6(c) matches the original better than the contours in Fig. 6(d). The fourth order PDE is more local. Both the second- and fourth-order PDE are able to smooth out the noise, as seen in the right part of the images. However, many of the "fine details" is also smoothed out by the second order PDE, but preserved by the fourth order PDE. In fact, the over-smoothing effect of the second order scheme is a problem in many applications.

(a) Original image

(b) Noisy image

(c) 4-order PDE

(d) 2-order PDE
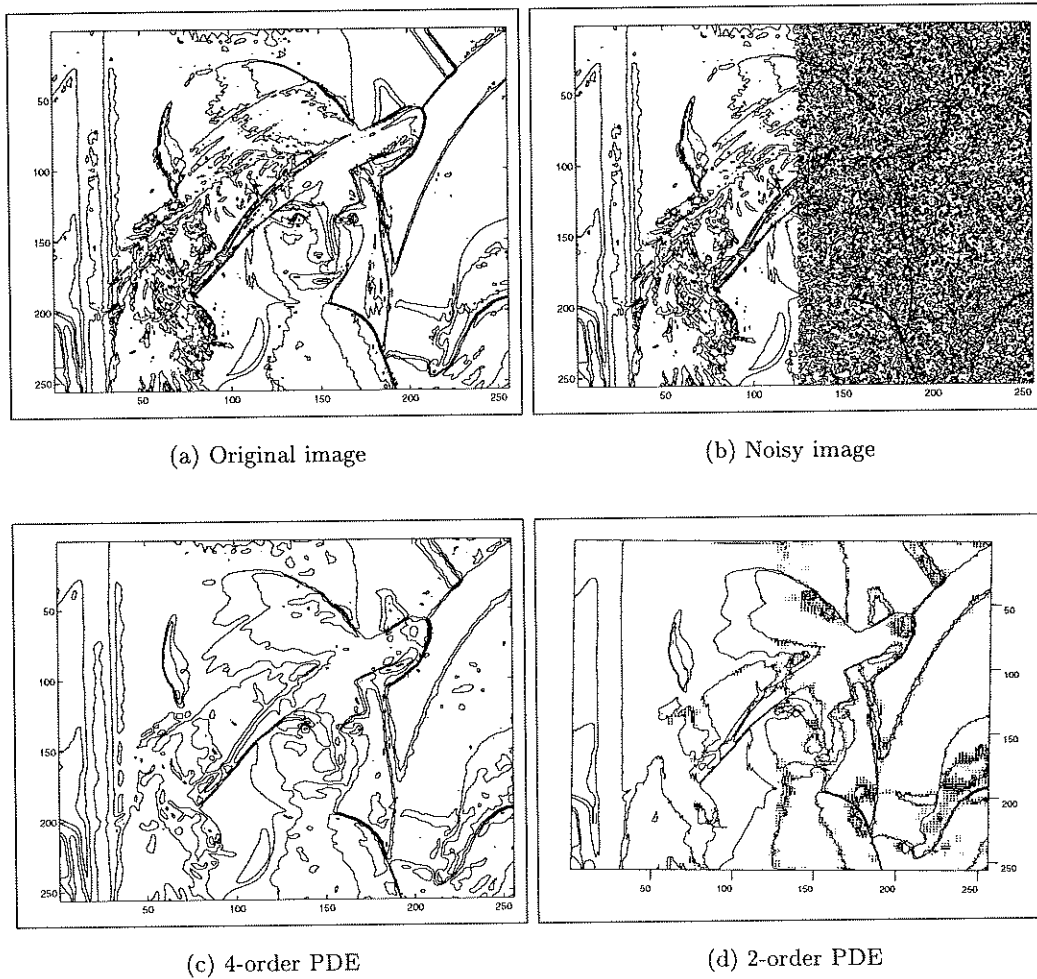
Fig. 6.   Evaluation of contour plot

In real life situations one usually do not have exact information about the noise level. Therefore, a perturbation of the exact noise level is used as input parameter in getting the results for Figure 7. The image consists of only two different intensity values (black and white). This image has been used as a test case in [13], [14], [16], [17], [18], [19]. The edges in the image are located along the vertical, the horizontal and the diagonal directions (cfr. Fig. 7). The details depicted in Fig. 7(f) demonstrate that the operator $g(u)$ works very locally along the edges.

(a) Original image   (b) Input SNR≈4   (c) Output: 4-order PDE

(d) Zoomed upper right corner of (a)

(e) Zoomed upper right corner of (b)

(f) Zoomed upper right corner of (c)
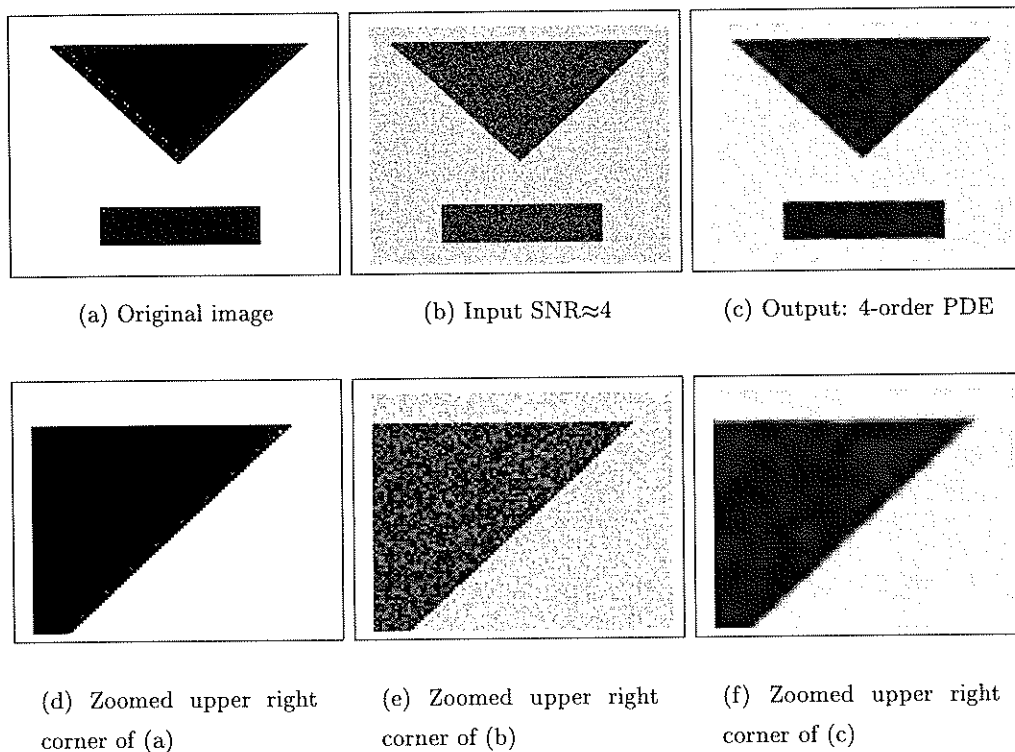
Fig. 7. 2D image evaluation

Our algorithm is trying to minimize the TV-norm of the gradient of the image functions. For simplicity of the implementations, we have dropped some of the terms with mixed derivatives. Our algorithm is not rotation-invariant. To evaluate that our algorthm is algorithmith respect to rotations, we rotate the image of Fig.7 by 20 degrees and then add some noise. The original, noise and smoothed image are shown in Fig.8.

(a) Original image   (b) Noisy image   (c) smoothed image
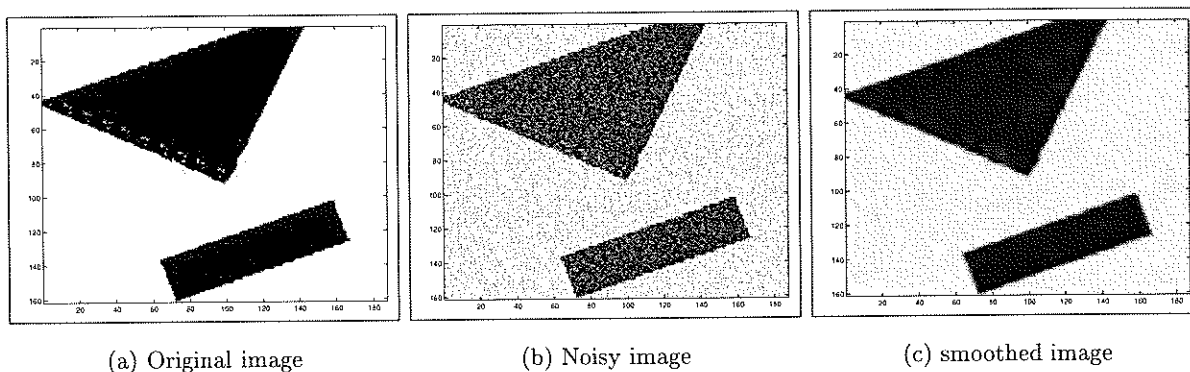
Fig. 8. 2D image evaluation of rotated object

Even our fourth order scheme is not rotation invariant it is clear from Fig.8 that the algorithm is able to recover the rotated image quite well. But we should mention that if a noisy version of the non-rotated image is used instead, the time step can be increased by a factor of 10.

In the next experiment, we want to show the capability of our algorithm for images with a smooth transition between different intensity regions and when the noise level is relative very large. In the figures signal-to-noise ratio (SNR) is used to denote SNR=S/σ_0, where σ_0 is the noise standard deviation and S is the average pixel intensity over a homogeneous region. In Fig.9, we have SNR$\approx$ 6.5 and in Fig.10, we have SNR$\approx$ 3.7.

(a) Original image   (b) Input SNR$\approx$6.5   (c) Output: 4-order PDE

Fig. 9.   2D image evaluation of a face
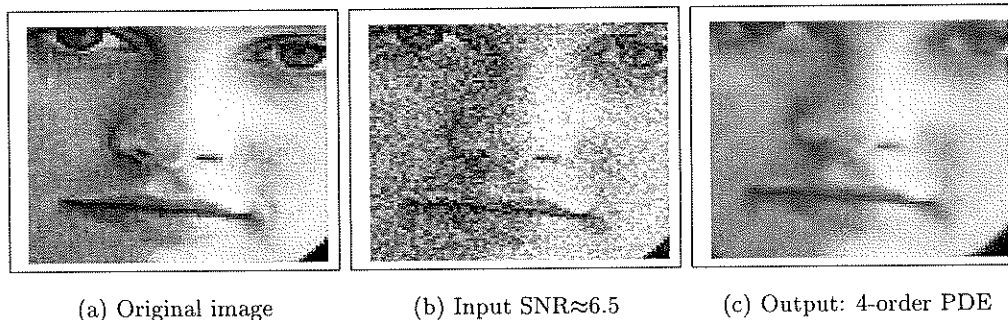
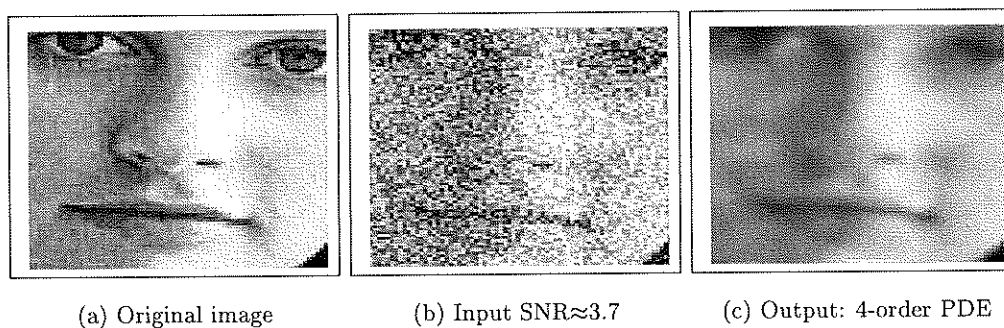(a) Original image   (b) Input SNR$\approx$3.7   (c) Output: 4-order PDE

Fig. 10.   2D image evaluation of a face

Even with an SNR of $\approx$3.7, the algorithm is able to reconstruct an image not too far from the original. Notice how well the upper part of the lip is taken care of. One of the difficulties with such noisy input data is that the algorithm have problems to find

homogeneous regions, and therefore the results gets poorer. Also in this experiment a perturbation of the exact noise level is used as input parameter.

In conclusion, these experiments demonstrate that our PDE method is robust, and the only prior information that goes into the algorithm is the approximate noise level of the input image. If we over estimate the noise level, i.e. the noise level we use is large than the actual noise level, then we will add more diffusion to the denoised image and the image will be much smoother. On the other hand, we will add less diffusion if we under estimate the noise level and the image will be less smoother.

B. Medical MRI images

Most digital 2D images have the same spatial resolution along the x and y directions. In this case (11) can be evaluated pixel by pixel. However, in medical MRI applications, volumetric (3D) images, and even time series of volume images (4D), are acquired. The spatial resolution cells of these volumes are very often non-isotropic. Moreover, in dynamic imaging the temporal sampling rate of the volume acquisitions will depend on the performance of the gradient system, pulse sequence characteristics, and the selected number of slices making up each volume in time. Fortunately, the difference scheme used to solve (11) can easily be modified to handle three spatial dimensions and time evolution in dynamic MR imaging. The user also has the opportunity to give different spatial and temporal resolution units as an input to the algorithm.

We shall first evaluate two different three-dimensional MRI datasets. Both datasets were acquired on a Siemens Vision 1.5 Tesla MR scanner.

In the previous section the reconstructed image is compared with the known original image. In the case of medical images, the evaluation of noise suppression is not that simple. The main problem is the lack of an original image to compare our result with. Therefore an acquisition-based noise reduction method is used to obtain the "ideal", or "true" image, as was also done in [2]. The "ideal" image is obtained by everaging 4 (AC=4) repeated measurements. For our algorithm, we just pick one of the 4 measurement and try to remove noise from it.

From [25] we know that Rician distribution approaches a Gaussian distribution at high SNR. By averaging over repeated measurements the SNR will increase and the Rice dis-

tribution should tend to a Gaussian distribution. This averaging process should therefor provide us with the desirable reference image.

The first MR data set consisted of isotropic $1 \times 1 \times 1$ mm^3 FLASH 3D head acquisitions from a healthy volunteer (fl3d_6b195.wkc, TR=20ms, TE=6ms, FA=30°, matrix=256x256, 32 slices). To our disposal we had the magnitude images from k-space averaged data using 1, 2, 3, and 4 measurements from the same slice positions. Input data to the algorithm is the data set with one measurement (AC=1, TA = 2min 46sec). The de-noised result is then compared to the observed average of four measurements (AC=4, TA = 10min 57sec), here taken to be the "ideal" image. The "ideal" image, the input image , and the output image produced by our algorithm are shown in Figs. 11(a),(b) and (c), respectively.

Due to the isotropic voxels in this data set, the partition $\Delta x = \Delta y = \Delta z$ is used in this calculation. One arbitrary slice from the 3D data set is given in Fig.11
The six transacted test-tubes located in the anterior part of the head coil were filled with reticulated foam and polystyrene spheres and used for texture analysis, reported elsewhere.

(a) AC=4   (b) Input AC=1   (c) Output: 4-order PDE
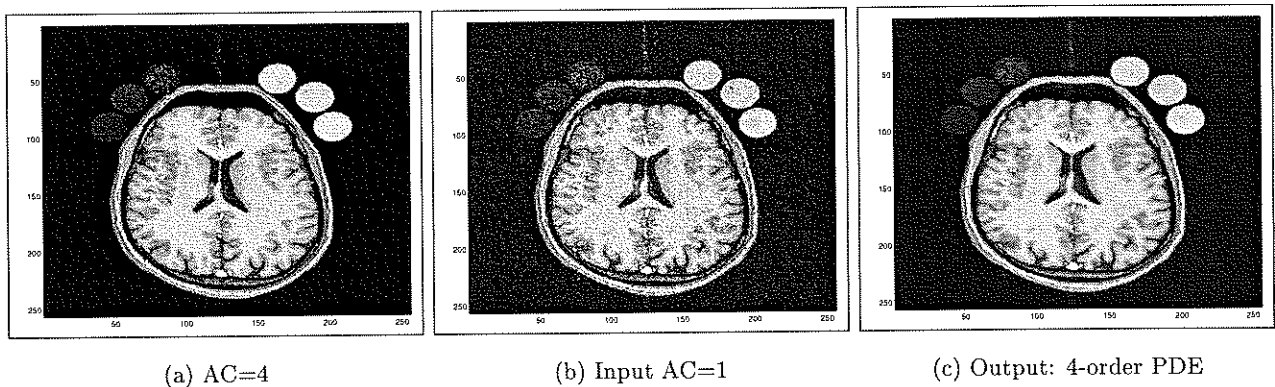
Fig. 11.   Evaluation of our smoothing algorithm, implemented for isotropic 3D images. Only one of the 32 contiguous slices, transectioning the lateral ventricles, is shown.

To better evaluate the performance of our algorithm, details from the same slice are depicted in Fig. 12 and Fig. 13.

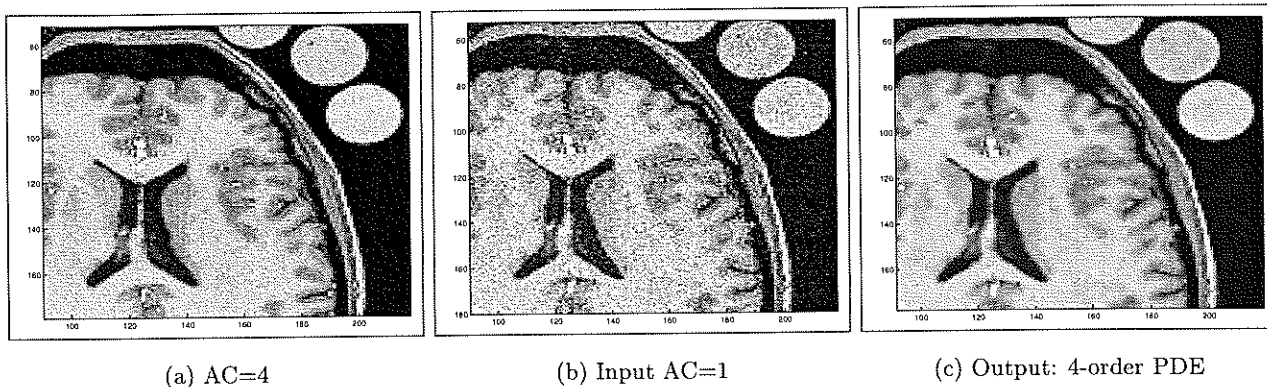(a) AC=4   (b) Input AC=1   (c) Output: 4-order PDE

Fig. 12. Detail from Fig. 11

On the anterior, right side of the head, three of the foam-filled test tubes are visible, and their content are recognized as rather homogeneous regions in Fig. 12(c). This is in accordance with the "ideal" image in Fig 12(a).

When zooming further, it is possible to see that even the image based on four measurements is affected by noise. The output from the restoration algorithm therefore seems to be even better than the "ideal" image.

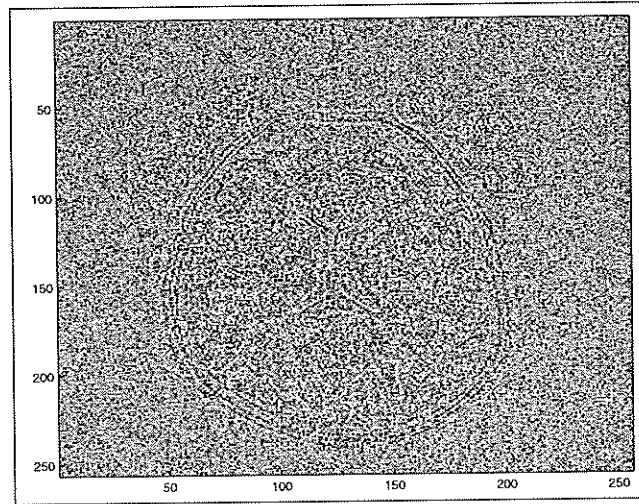(a) AC=4   (b) Input AC=1   (c) Output: 4-order PDE
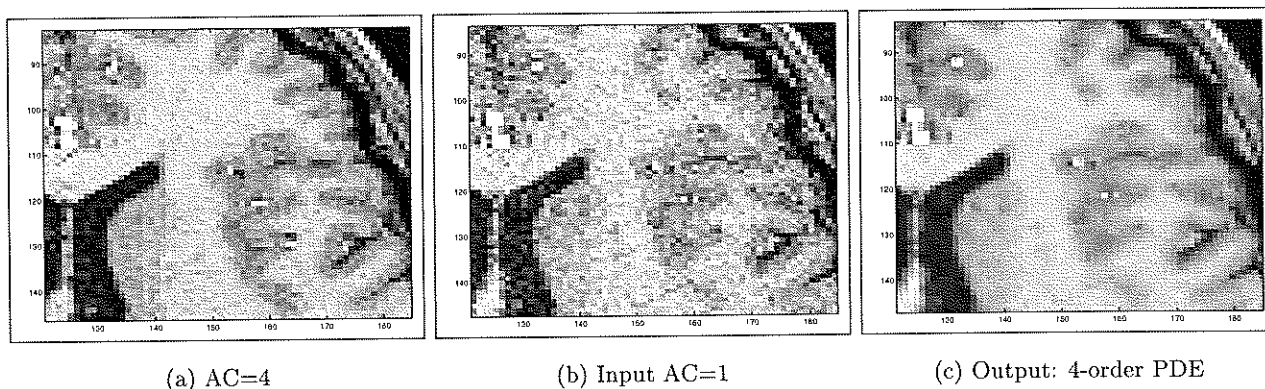
Fig. 13. Detail from Fig. 12

In addition to visual comparison of the output with the "ideal" image, we have also computed the difference between the input and the output. This will better reveal where details have been lost. The difference image is shown in Fig. 14.

(a) Difference image

Fig. 14. Difference between input and output image, i.e. Fig. 11: (b) - (c).

Here, it is easy to see that the major difference between input and output is noise, as it should be. However, some weak contours of the skull and the test tubes can be seen, showing that our de-noiser have a slight smoothing effect also at tissue boundaries.

The second MRI data set is from an MR phantom consisting of a tube filled with plastic straws embedded in Gd-doped agarose gel with tissue equivalent T1 and T2 relaxation times. This straws phantom was imaged with a spin-echo (SE) pulse sequence using the same MR scanner as above (TR=150ms, TE=15ms, FOV=75x150mm^2, matrix=256x512, thick=2mm, 5 slices). The SE pulse sequence was designed to generate 8 single measurements together with 7 k-space averages from measurements 1+2, 1+2+3, ... ,1+2+...+8, respectively, before magnitude images were calculated (cf. [33]). We applied our restoration algorithm to one of the eight single-measurement datasets (AC=1), which all had poor SNR compared to the seven averaged data sets. The results are then compared with the observed average of eight SE measurements, taken to represent the "ideal" image.
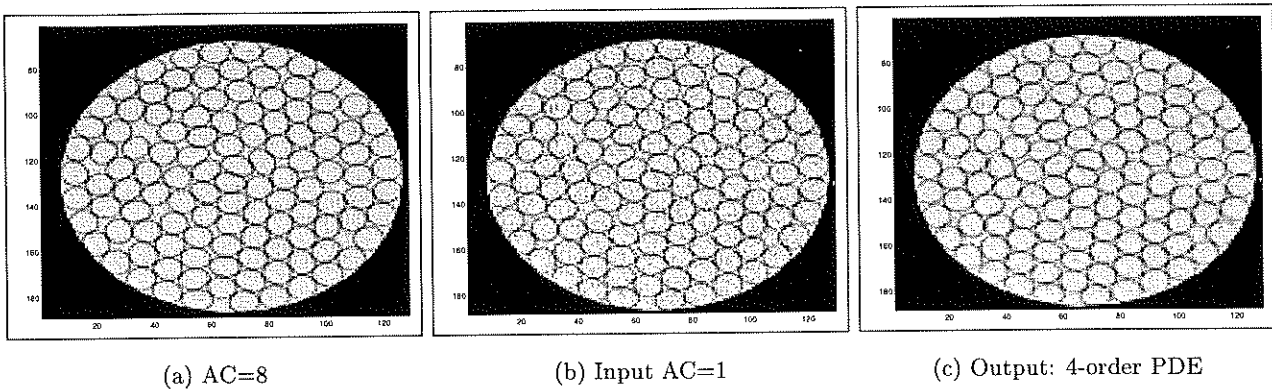
(a) AC=8   (b) Input AC=1   (c) Output: 4-order PDE

Fig. 15. The plastic straws MR phantom used to test our de-noiser's preservation of edge information. Each pixel is approximately 0.15 x 0.30 mm^2. The k-space average of eight measurements (AC=8) was taken to represent the "ideal" image. Only one of the five transaxial slice images is shown.

This peculiar, high spatial resolution data set is chosen to test if our restoration algorithm is capable to work as locally as it should. Notice how thin the straws walls are in Fig. 15. These tiny, circular contours could thus be sensitive to all kind of algorithmic influence and smoothing effects of our de-noiser. Figure 16 shows the results in more detail.

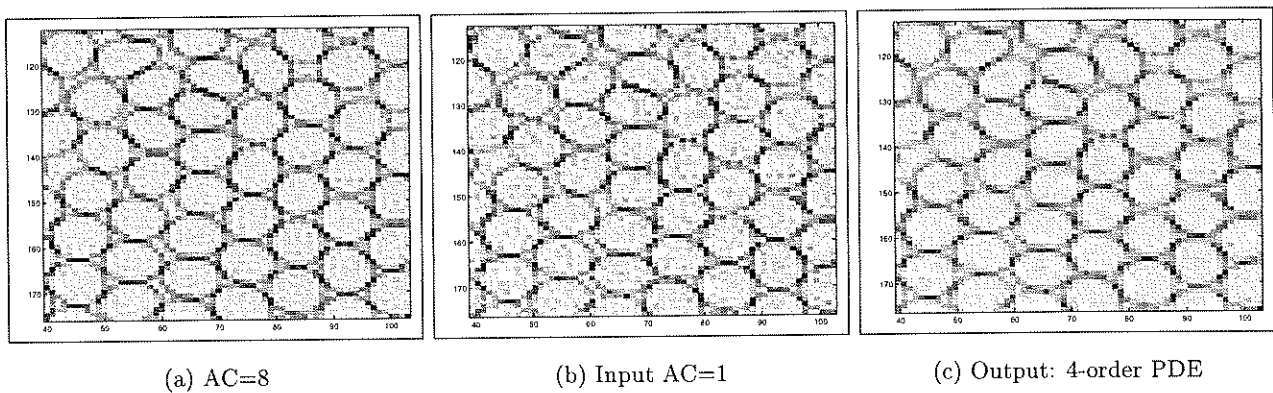(a) AC=8   (b) Input AC=1   (c) Output: 4-order PDE

Fig. 16. Detail from de-noising of the high spatial resolution straws phantom image.

For parabolic PDE based noise removal algorithms a common problem is that the reconstructed image will be a little blurred, because every pixel is somehow influenced by the surrounding ones in each iteration, as seen from (12). From the results depicted in

Fig. 16, it is clear that our restoration algorithm preserves the thin walls very well, while the interior of the straws are getting smoothed. The de-noised image is remarkably similar to the "ideal" image, which have almost three times ($\sqrt{8}$) better SNR than the input image.

A desirable generalization of our noise removal algorithm is to include the time domain as well, such that it could work on time series of images (e.g. 2D+time) obtained from dynamic or functional MRI examinations. Time series of images are obtained in various situations, such as fMRI brain activation studies using the so-called Blood Oxygenation Level Dependent (BOLD) contrast technique, and for tracking a bolus of intravenously injected contrast agent while it passes through a vascular tree or a capillary bed in breast, prostate, kidney, heart or brain.

We have tested a spatio-temporal implementation of our de-noiser on a routine brain perfusion study. We used 3D+time data from a gradient-echo echo-planar imaging (GE EPI) sequence on a Siemens Vision 1.5 T scanner (TR=2000ms, TE=60.73ms, FA=90°, FOV=240mm x240mm, matrix=96x128, slice thickness=5mm, inter-slice gap=1.5mm).

Fifteen slices were repeatedly measured every 2 second, for a period of 1 min and 20 second, such that each slice were scanned 50 times in succession. After about three measurements a rapid injection of an MR contrast agent was injected intravenously. As the bolus passed the microcirculation of the brain, a magnetic susceptibility-induced signal drop could be observed in those voxels covering perfused brain tissue. Due to expensive computation of 4D data, we selected one slice, transacting the brain at the level of the lateral ventricles, and applied our 2D+time de-noising algorithm to this image time series. In the upper part of Fig. 17 this slice is shown at time $t = 0$. In the lower part, the signal intensity versus time from a selected pixel is shown. Tissue covered by this pixel is clearly perfused as we see a marked decrease in signal intensity from time frame 10, with signal minimum about 20 s (frame 13) after bolus injection.

Another (annoying) source for the variation in the pixel time course is noise. Notice how the signal oscillates even before the contrast agent has reached the brain (frame 1 to frame 8), and it is also hard to decide where in time the signal recovers towards baseline

after bolus passage. Since estimation of local cerebral blod flow (rCBF), local cerbral blood volume (rCBV), and mean transit time (MTT) of plasma in the capillary bed is essentially dependent on the decision of start and stop points in time for the signal drop, and also on the area under the signal intensity curve during bolus passage, time-course restoration and proper de-noising will be very helpful.

In this medical context, we therefor tested our $3D$ (i.e. $2D$ and *time*) noise removal algorithm with different weight for smoothing in time and space.
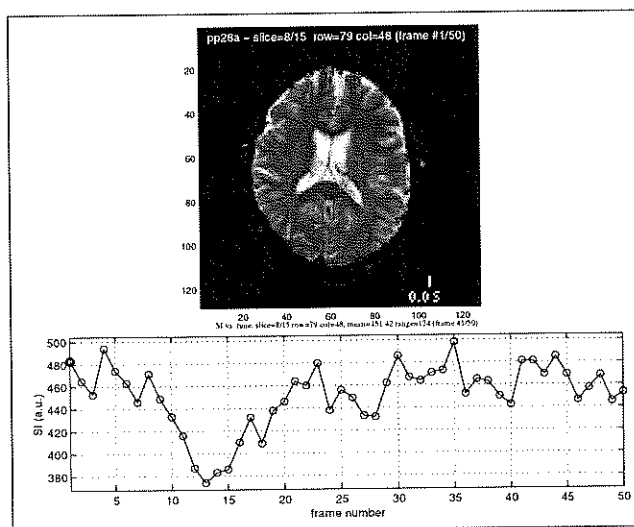
(a) One pixel evaluated in time

Fig. 17. 2D+time evaluation

In contrast to previous cases, we do not have an "ideal" time course to use in an evaluation. Even worse, the injected contrast agent forces each pixel to change its signal in time, and recirculation and leaking effects might occur, so averaging over repeated measurement would not be feasible. However, we would expect in the "ideal" situation that the pixel-intensities should be almost constant both before and after the signal drop due to bolus passage. If the restored image time-series approaches this "ideal" situation we would judge the method to be potentially useful. Another method to assess the goodness of de-noising is to compute and display the difference between the observed time course and the restored time course.

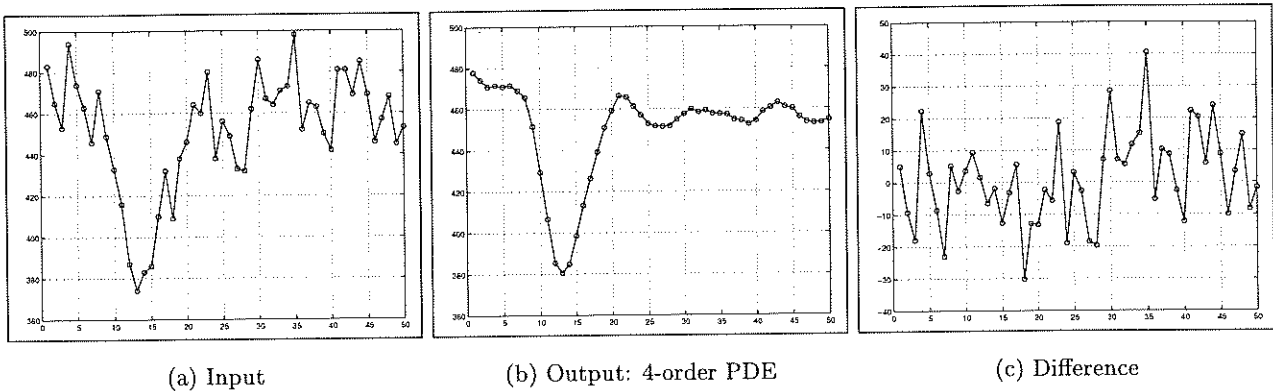(a) Input   (b) Output: 4-order PDE   (c) Difference

Fig. 18. 2d+time evaluation

The measured perfusion time series and the PDE smoothed time series are given in Fig. 18 (a) and (b), respectively. Notice how easy it is to estimate the start and the end of the V-shaped signal drop in the output. We will also remark how well the minimum point of the signal drop is preserved. The fast oscillating signals in Fig. 18 (c) indicate that main difference between input and output is noise.

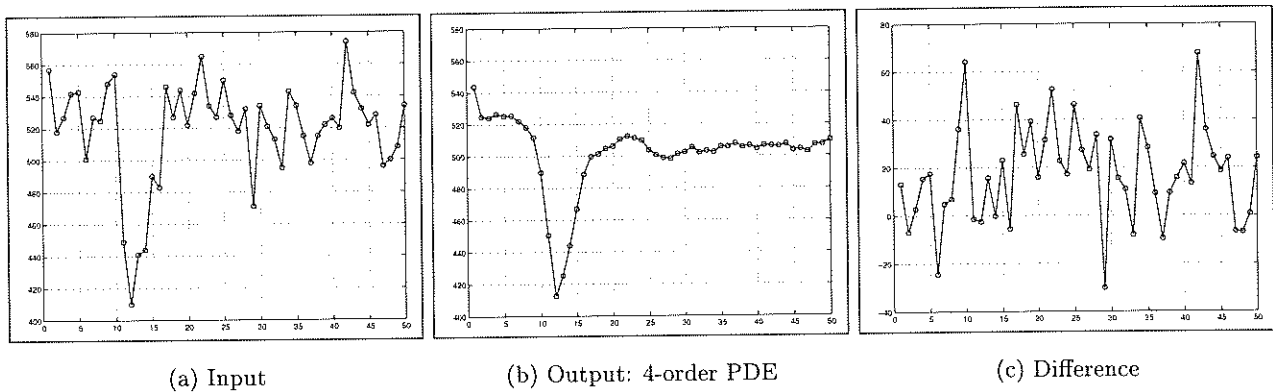(a) Input   (b) Output: 4-order PDE   (c) Difference

Fig. 19. 2d+time evaluation

In Fig. 19 another pixel time-course is evaluated. In order to retain the minimum point in the V-shaped curve, the pixel-intensity is unfortunately not constant from slice 20-50, but it is a big improvement from the input data.

We would like to add that our algorithm seems to work for a large set of perfusion pixel

time-courses being tested. A next step will therefore be to conduct a more rigorous evaluation on a larger set of perfusion examinations. To be relevant for clinical use, estimation of the physiological parameters described above (e.g. [34]), should also be incorporated.

VIII. Concluding Remarks

In this paper we have developed a fourth-order PDE model for noise suppression that is tested on a broad range of medical magnetic resonance images as well as on non-medical test images. Our algorithm demonstrates good preservation of edges and contours without smoothing out important anatomical or functional detail, even at poor signal-to-noise ratios. We have also compared our method with a related second-order PDE model and find our method to perform overall better on the images being tested.

To compute a de-noised version of the input data, the user has only to specify a rough estimate of the noise level which can be fixed for a certain type of MR examination or pulse sequence. The algorithm is applicable to both 2D and 3D anatomical images as well as time series of planer and volumetric images. Such 2D+time or 3D+time images result from dynamic and functional MRI examinations, which are becoming increasingly important in clinical practice. Moreover, our method allows the step-size in the x, y, z, and t directions to be adjusted according to the pulse sequence being used and thereby the spatial anisotropy of the voxels and the temporal sampling rate, in case of dynamic imaging.

A next step will be to investigate the de-noising effect in relation to state-of-the-art tissue classification and physiological parameter estimation procedures (e.g. SPM [35], [36], [37], AFNI [38], [39], FreeSurfer [40], [41], Makeperf [34]). In this evaluation both simulated data (e.g. BrainWeb simulated brain database [42], [43]) and real MRI data from medical routine should be used, and our method should be compared to a carefully selected set of competing de-noising algorithms that works in both space and time.

Acknowledgments

References

[1] E. M. Haacke, R. W. Brown, M. R. Thompson, and R. Venkatesan, *Magnetic Resonance Imaging: Physical Principles and Sequence Design*, Wiley, New York, 1999.

[2] F. Godtliebsen, *A Study of Image Improvement Techniques Applied to NMR Images*, Ph.D. thesis, The Norwegian Institute of Technology (NTNU), Division of Mathematical Sciences, September 1989.

[3] F. Godtliebsen, "Noise reduction using Markov random fields," *Journal of Magnetic Resonance*, vol. 92, pp. 102–, 1991.

[4] A. Lundervold and F. Godtliebsen, "Noise reduction and brain tissue classification in MR images," in *Proceedings of the 1992 IEEE Nuclear Science Symposium and Medical Imaging Conference*, Orlando, FL, October 25-31 1992, pp. 1265–1267.

[5] H. Soltanian-Zadeh, J. P. Windham, and A. E. Yagle, "A multidimensional nonlinear edge-preseriving filter for magnetic resonance image restoration," *IEEE Transactions on Image Processing*, vol. 14, no. 2, pp. 147–161, 1995.

[6] H. Soltanian-Zadeh, "Feature space analysis in MRI," in *Signal Processing for Magnetic Resonance Imaging and Spectroscopy*, H. Yan, Ed., pp. 255–315. Marcel Dekker, New York, 2002.

[7] A. Perona and J. Malik, "Scale-space and edge detection using anisotropic diffusion," *IEEE Transactions on Pattern Analysis and Machine Intelligence*, vol. 12, no. 7, pp. 629–639, 1990.

[8] G. Gerig, O. Kubler, R. Kikinis, and F. Jolesz, "Nonlinear anisotropic filtering of MRI data," *IEEE Transactions on Medical Imaging*, vol. 11, no. 2, pp. 221–2232, 1992.

[9] M. J. Black, G. Sapiro, D. H. Marimont, and D. Heeger, "Robust anisotropic diffusion," *IEEE Transactions on Image Processing*, vol. 7, no. 3, pp. 421–432, 1998.

[10] A. B. Hamza and H. Krim, "A variational approach to maximum a posteriori estimation for image denoising," in *Energy Minimization Methods in Computer Vision and Pattern Recognition*, M. A. T. Figueiredo, J. Zerubia, and A. K. Jain, Eds., Third International Workshop, Sophia Antipolis, France, September 3-5, 2001 2001, pp. 19–34.

[11] L. I. Rudin, S. Osher, and E. Fatemi, "Nonlinear total variation based noise removal algorithms," *Physica D*, vol. 60, pp. 259–268, 1992.

[12] M. E. Alexander, R. Baumgartner, A. R. Summers, C. Windischberger, M. Klarhoefer, E. Moser, and R. L. Somorjai, "A wavelet-based method for improving signal-to-noise ratio and contrast in MR images," *Magnetic Resonance Imaging*, vol. 18, no. 2, pp. 169–180, 2000.

[13] L. Alvarez, P.-L. Lions, and J.-M. Morel, "Image selective smoothing and edge detection by nonlinear diffusion:II," *SIAM Journal of Numerical Analysis*, vol. 29, no. 3, pp. 845–866, 1992.

[14] P. Blomgren, T. F. Chan, P. Mulet, L. Vese, and W. L. Wan, "Variational PDE models and methods for image processing," in *Numerical analysis 1999 (Dundee)*, pp. 43–67. Chapman & Hall/CRC, Boca Raton, FL, 2000.

[15] F. Catt, P.-L. Lions, J.-M. Morel, and T. Coll, "Image selective smoothing and edge detection by nonlinear diffusion," *SIAM Journal of Numerical Analysis*, vol. 29, pp. 182–193, 1992.

[16] Antonin Chambolle, "Image segmentation by variational methods: Mumford and Shah functional and the discrete approximations," *SIAM J. Appl. Math.*, vol. 55, no. 3, pp. 827–863, 1995.

[17] Antonin Chambolle and Pierre-Louis Lions, "Image recovery via total variation minimization and related problems," *Numer. Math.*, vol. 76, no. 2, pp. 167–188, 1997.

[18] Tony F. Chan, Gene H. Golub, and Pep Mulet, "A nonlinear primal-dual method for total variation-based image restoration," *SIAM J. Sci. Comput.*, vol. 20, no. 6, pp. 1964–1977 (electronic), 1999.

[19] T. Chan, A. Marquina, and P. Mulet, "High-order total variation-based image restoration," *SIAM Journal on Scientific Computing*, vol. 22, no. 2, pp. 503–516 (electronic), 2000.

[20] K. Majava, *Optimization-based techniques for image restoration*, Ph.D. thesis, University of Jyvaskyla, Finland, 2001.

[21] Y.-L. You and M. Kaveh, "Fourth-order partial differential equation for noise removal," *IEEE Transactions on Image Processing*, vol. 9, no. 10, pp. 1723–1730, 2000.

[22] J. Greer and Bertozzi A., "H^1 solutions of a class of fourth order nonlinear equations for image processing," Preprint, 2002.

[23] T. Tasdizen, R. Whitaker, P. Burchard, and S. Osher, "Geometric surface processing via normal maps," Tech. Rep. 02-3, UCLA, Applied Mathematics, 2002, Available at http://www.math.ucla.edu/applied/cam/index.html.

[24] M. Lysaker, "Noise reduction in MR images," M.S. thesis, University of Bergen, Department of Matrhematics and Department of Physiology, December 2000, (in Norwegian).

[25] J. Sijbers, A. J. den Dekker, J. Van Audekerke, M. Verhoye, and D. Van Dyck, "Estimation of the noise in magnitude MR images," *Magnetic Resonance Imaging*, vol. 16, no. 1, pp. 87–90, 1998.

[26] R. D. Nowak, "Wavelet-based Rician noise removal for magnetic resonance imaging," *IEEE Transactions on Image Processing*, vol. 8, no. 10, pp. 1408–1419, 1999.

[27] W. S. Hinshaw and A. H. Lent, "An introduction to NMR imaging: From the Bloch equation to the imaging equation," *Proceedings of the IEEE*, vol. 71, pp. 338–350, 1983.

[28] Parker D. L. and G. T. Gullberg, "Signal-to-noise efficiency in magnetic resonance imaging," *Medical Physics*, vol. 17, no. 2, pp. 250–257, 1990.

[29] Paul T. Callaghan, *Principles of Nuclear Magnetic Resonance Microscopy*, Oxford University Press, Oxford, 1991.

[30] R. M. Henkelman, "Measurement of signal intensities in the presence of noise in MR images," *Medical Physics*, vol. 12, no. 2, pp. 232–233, 1985.

[31] A. Macovski, "Noise in MRI," *Magnetic Resonance in Medicine*, vol. 36, no. 3, pp. 494–497, 1996.

[32] I. A. Cunningham and R. Shaw, "Signal-to-noise optimization of medical imaging systems," *Journal of The Optical Society of America, Series A*, vol. 16, no. 3, pp. 621–632, 1999.

[33] A. M. Fenstad, A. Lundervold, M. Bock, and L. R. Schad, "How does signal-to-noise ratio influence texture

measure?," in *Proceedings of the Eighth Annual Scientific Meeting of the International Society for Magnetic Resonance in Medicine*, Denver, CO, April 1-7 2000, p. 61.

[34] A. G. Sorensen and R. Reimer, *Cerebral MR Perfusion Imaging - Principles and Current Applications*, Thieme, Stuttgart, 2000.

[35] SPM, "http://www.fil.ion.ucl.ac.uk/spm/," .

[36] J. Ashburner and K. J. Friston, "Voxel-based morphometry - the methods," *NeuroImage*, vol. 11, pp. 805–821, 2000.

[37] K. J. Friston, P. Jezzard, and R. Turner, "Analysis of functional MRI time series," *Human Brain Mapping*, vol. 1, pp. 153–171, 1994.

[38] AFNI, "http://afni.nimh.nih.gov/afni/," .

[39] R. W. Cox and J. S. Hyde, "Software tools for analysis and visualization of FMRI data," *NMR in Biomedicine*, vol. 10, pp. 171–178, 1997.

[40] FreeSurfer, "http://surfer.nmr.mgh.harvard.edu/," .

[41] A. M. Dale, B. Fischl, and M. I. Sereno, "Cortical surface-based analysis I: Segmentation and surface reconstruction," *NeuroImage*, vol. 9, pp. 179–194, 1999.

[42] BrainWeb, "http://www.bic.mni.mcgill.ca/brainweb/," .

[43] R. K. S. Kwan, A. C. Evans, and G. B. Pike, "MRI-simulation-based evaluation of image-processing and classification methods," *IEEE Transactions on Medical Imaging*, vol. 18, no. 11, pp. 1085–1097, 1999.

[44] COST B11, "http://www.uib.no/costb11/," .